Cellular and Molecular Life Sciences (2025) 82:32
https://doi.org/10.1007/s00018-024-05565-w

ORIGINAL ARTICLE

Microtubule acetylation and PERK activation facilitate eribulin-induced mitochondrial calcium accumulation and cell death

Seongeun Song[1] · Panseon Ko[1] · Seula Keum[1] · Jangho Jeong[1] · Ye Eun Hwang[1] · Minwoo Lee[1] · Jee-hye Choi[1] · Youn-Sang Jung[1] · Sung Hyun Kim[2,3] · Sangmyung Rhee[1]

Received: 1 May 2024 / Revised: 3 December 2024 / Accepted: 23 December 2024

Abstract

Over the past few decades, microtubules have been targeted by various anticancer drugs, including paclitaxel and eribulin. Despite their promising effects, the development of drug resistance remains a challenge. We aimed to define a novel cell death mechanism that targets microtubules using eribulin and to assess its potential in overcoming eribulin resistance. Notably, treating non-resistant breast cancer cells with eribulin led to increased microtubule acetylation around the nucleus and cell death. Conversely, eribulin-resistant (EriR) cells did not exhibit a similar increase in acetylation, even at half-maximal inhibitory concentrations. Interestingly, silencing the *ATAT1* gene, which encodes the α-tubulin N-acetyltransferase 1 (the enzyme responsible for microtubule acetylation), induces eribulin resistance, mirroring the phenotype of EriR cells. Moreover, eribulin-induced acetylation of microtubules facilitates the transport of Ca^{2+} from the ER to the mitochondria, releasing cytochrome c and subsequent cell death. Transcriptome analysis of EriR cells revealed a significant downregulation of ER stress-induced apoptotic signals, particularly the activity of protein kinase RNA-like ER kinase (PERK), within the unfolded protein response signaling system. Pharmacological induction of microtubule acetylation through a histone deacetylase 6 inhibitor combined with the activation of PERK signaling using the PERK activator CCT020312 in EriR cells enhanced mitochondrial Ca^{2+} accumulation and subsequent cell death. These findings reveal a novel mechanism by which eribulin-induced microtubule acetylation and increased PERK activity lead to Ca^{2+} overload from the ER to the mitochondria, ultimately triggering cell death. This study offers new insights into strategies for overcoming resistance to microtubule-targeting agents.

Keywords Microtubule acetylation · Eribulin · Drug resistance · Calcium transfer · ER-mitochondria contact · PERK signaling

Introduction

Microtubules, which are dynamic cytoskeleton components, comprise α- and β-tubulin heterodimers essential for cellular functions such as mitosis, motility, and intracellular transport [1, 2]. They form structural networks linked to membrane-bound organelles such as lysosomes, endoplasmic reticulum (ER), and mitochondria [3]. Post-translational modifications (PTMs) such as phosphorylation, detyrosination, and acetylation modulate their functionality [4]. Notably, acetylation at lysine 40 of α-tubulin plays a crucial role in ER sliding events and dynamic ER-mitochondria interactions [5]. The link between microtubule acetylation and cellular stress responses has also been well-documented. For instance, microtubule acetylation is critical for adaptation to tunicamycin-induced ER stress in MDA-MB-231 (MDA-231) breast cancer cells [6]. Additionally, oxidative stress-induced microtubule acetylation promotes amyloid-beta (Aβ) secretion by facilitating the peripheral localization of neutralized lysosomal vesicles. In the 5xFAD transgenic mouse model of Alzheimer's disease, where microtubule acetylation was increased by LPS, reducing these levels through *ATAT1* knockdown (KD) resulted in decreased Aβ plaque deposition and memory loss [7]. Thus, understanding

✉ Sangmyung Rhee
sangmyung.rhee@cau.ac.kr

1 Department of Life Science, Chung-Ang University, Seoul 06974, Republic of Korea

2 Department of Neuroscience, Graduate School, Kyung Hee University, Seoul 02447, Korea

3 Department of Physiology, School of Medicine, Kyung Hee University, Seoul 02447, Korea

Published online: 31 December 2024

the role of microtubule acetylation in cellular adaptation to various stressors is crucial.

Among the numerous anticancer drugs available for breast cancer treatment, microtubule-targeting agents (MTAs) play a pivotal role in inhibiting mitosis by modulating microtubule dynamics. This regulation curtails the uncontrolled proliferation of cancer cells and promotes cell death. The genesis of MTAs traces back to the approval of vinblastine sulfate by the U.S. Food and Drug Administration (FDA) approval in 1961. Subsequently, extensive clinical trials have been conducted, consistently resulting in FDA approval for the use of these agents in breast cancer patients [8]. However, the emergence of drug resistance in cancer cells progresses rapidly, accounting for 90% of tumor-related deaths and a major cause of recurrence and metastasis [9–13]. For instance, in triple-negative breast cancer (TNBC) cells, overexpression of synaptotagmin-like 4 heightens microtubule dynamics, diminishing microtubule acetylation levels and conferring resistance to paclitaxel [14]. Consequently, eribulin was approved by the FDA in 2010 for breast cancer patients unresponsive to first- and second-line chemotherapy. Eribulin binds to the plus-ends of microtubules, inhibiting their growth [15, 16]. Nevertheless, resistance to eribulin can also emerge in breast cancer cells [17]. Therefore, investigating the mechanism of cell death induced by microtubule-targeting anticancer drugs, including eribulin, remains vital in surmounting drug resistance.

Within the mitochondria-associated membrane (MAM), a specialized microdomain situated between the outer mitochondrial membrane (OMM) and the ER membrane, critical biological processes such as lipid biosynthesis, autophagosome initiation, and Ca^{2+} transfer occur [18–20]. Excessive Ca^{2+} transfer from the ER to the mitochondria within this microdomain can promote cell death by triggering the opening of the mitochondrial permeability transition pore, leading to the release of pro-apoptotic proteins such as cytochrome c and eventual cell demise [21]. The efficiency of Ca^{2+} transfer is influenced by the proximity between the ER and mitochondria, with reports suggesting that an increased distance within the MAM can impede Ca^{2+} transfer, thereby reducing Ca^{2+}-dependent apoptosis and mitigating drug sensitivity to mitotane or bortezomib [20, 22]. Additionally, Ca^{2+} transfer is regulated by the unfolded protein response (UPR) signaling pathway, activated in response to ER stress induced by cellular stress such as chemotherapy. This pathway, involving protein kinase RNA-activated-like ER kinase (PERK), inositol requiring enzyme 1α (IRE1α), and activating transcription factor 6, is triggered to alleviate stress. However, sustained ER stress can lead to cell death [23]. Notably, PERK and IRE1α interact with MAM-localized proteins, such as inositol-1, 4, 5-triphosphate receptor and Mitofusin 2 (MFN2), which modulate Ca^{2+} transfer to mitochondria. Downregulation of PERK and IRE1α reduces Ca^{2+} transfer from the ER to the mitochondria [24, 25]. However, comprehensive studies elucidating how the coordination of structural changes in the ER and mitochondria and UPR signaling facilitates Ca^{2+} transfer upon anticancer drug treatment remain elusive.

In this study, we found that the upregulation of microtubule acetylation by eribulin was pivotal in counteracting eribulin resistance. Eribulin not only enhanced microtubule acetylation near the nucleus but also augmented the connections between the ER and mitochondria. This increased connectivity facilitated excessive Ca^{2+} transfer, ultimately triggering cell death. Our bioinformatics analysis of eribulin-resistant (EriR) cells revealed that the activation of PERK activity, a component of the UPR triggered by ER stress, was essential for eribulin-induced cell death. Furthermore, we demonstrated that the combination treatment with tubacin, which boosts microtubule acetylation, and CCT020312, a PERK activator, significantly induced cell death in EriR cells and a xenograft model using EriR cells. Overall, our investigation delved into the interplay among eribulin, microtubule acetylation, and cellular dynamics to elucidate the potential mechanism of eribulin resistance and propose novel strategies for its mitigation in EriR breast cancer cells.

Materials and methods

Cell culture and transfection

The human breast cancer cell lines MDA-231 was purchased from the Korea Cell Line Bank (Seoul, South Korea). In contrast, the Hs578T cell line, a TNBC cell line frequently used in studies of aggressive breast cancer phenotypes due to mesenchymal characteristics, was obtained from Woo Keun Song (Gwangju Institute of Science and Technology). MDA-231 cells were cultured in Roswell Park Memorial Institute 1640 medium (RPMI 1640; #31800022; Gibco-BRL, Grand, NY, USA) supplemented with 10% fetal bovine serum (FBS; # US-FBS-500; GW Vitek, Seoul, South Korea), 100 units/mL penicillin, and 100 µg/mL streptomycin (#LS202-02; WelGENE, Daegu, South Korea). Hs578T was cultured in Dulbecco's Modified Eagle's Medium (DMEM; #12100046; Gibco-BRL) supplemented with 10% FBS, 100 units/mL penicillin, and 100 µg/mL streptomycin. All cell lines were incubated at 37 °C and 5% CO_2 conditions. For transient transfection, 2.5 µg of plasmids were transfected into MDA-231 and Hs578T cells using Lipofectamine 2000 Reagent (#11668019; Invitrogen, Carlsbad, CA, USA) according to the manufacturer's instructions.

Plasmids construction

End-binding 1 (GFP-EB1) (#KE0822_mNEGFP) and SEC61 translocon subunit beta (pCNS-SEC61B) (#KU001654) were obtained from the Korea Human Gene Bank (Daejeon, Korea). SEC61B was cloned into pEGFP-C1 (#6084-1; Clontech, Palo Alto, CA, USA) and mRFP-C1 (#54764; Addgene, Cambridge, MA, USA). Mito-GCaMP6f and ER-GCaMP6-150 were provided by Sung Hyun Kim (Kyung Hee University). Expression vectors were generated through restriction enzyme digestion. Lentiviral shRNA oligonucleotides were employed, including human *ATAT1* shRNA #1 (5′-ACCGCACCAACTGGCAATTGA-3′), and shRNA #5 (5′-AACCGCCATCTTCTTTATATTT-3′) targeting the coding region of *ATAT1*, human *ERN1* shRNA (5′-AGGGCCTGGTCACCACAATTA-3′) targeting the 3′UTR of *ERN1*, human *EIF2AK3* shRNA (5′-TAGCAGCAATCC CTAATATAT-3′) targeting the 3′UTR of *EIF2AK3*, and human *HDAC6* shRNA (5′- CATCCCATCCTGAATATC CTT-3′). These shRNA oligos were cloned into the pLKO.1-blast vector (#26655; Addgene). For *ATAT1* overexpression, the coding sequence (CDS) of *ATAT1* was obtained by PCR using pEF5B-FRT-GFP-αTAT1 (#20799, Addgene), and cloned into the pcDNA6/myc-His A expression vector (#V22120; Invitrogen). Subsequently, myc-*ATAT1* cDNA was generated by PCR from the pcDNA6/myc-His A-*ATAT1* construct and cloned into the pLenti-blasticidin vector to create a lentiviral expression vector.

Antibodies and reagents

The following antibodies were purchased from Cell Signaling Technology (MA, USA): Acetyl-α-tubulin (#5335), PERK (#5683), IRE1α (#3294), CHOP (#2895), cleaved PARP (#5625), cleaved caspase-9 (#20750), and cleaved caspase-3 (#9661). Phospho-IRE1 alpha (S724; #NB100-2323) was obtained from Novus Biologicals (Littleton, CO, USA), while phospho-PERK (T982; #ab192591) was purchased from Abcam (Cambridge, USA). Alpha-tubulin (#sc-5286), cytochrome c (#sc-13156), and GAPDH (#sc-32233) antibodies were purchased from Santa Cruz Biotechnology (Dallas, TX, USA), and detyrosinated anti-tubulin antibody (#AB3201) was acquired from Millipore (Burlington, MA, USA). α-tubulin (#T9026) was purchased from Sigma-Aldrich (St. Louis, MO, USA). Delta-2 tubulin (#PAB0202) was purchased from Covalab (Villeurbanne, France). Horseradish peroxidase (HRP)-conjugated goat anti-rabbit (#111-035-006), HRP-conjugated goat anti-mouse (#115-035-006), FITC-conjugated goat anti-mouse (#115-095-003), and Cy3-conjugated donkey anti-mouse (#715-165-150) were purchased from Jackson ImmunoResearch Laboratories (West Grove, PA, USA). Alexa Flour 488 goat anti-rabbit was purchased from Invitrogen (#A-11008). All the antibodies were used for western blotting and immunocytochemical analyses. Eribulin (E7389; Eisai, Tokyo, Japan), tubacin (#537049-40-4; Cayman Chemicals, Ann Arbor, MI, USA and #S2239; Selleckchem, Houston, TX, USA), CCT020312 (#324879; Sigma-Aldrich), thapsigargin (#T9033; Sigma-Aldrich), adenosine 5′-Triphosphate (γ−32P; #BLU502Z500UC; PerkinElmer, Boston, MA, USA), ionomycin, (#I24222; Invitrogen) and MitoTracker Red CMXRos (#9082; Cell Signaling Technology) were used for experiments.

Western blotting

Cells were rinsed with cold phosphate-buffered saline (PBS) and lysed using lysis buffer containing 2% NP-40, 1% sodium dodecyl sulfate, 150 mM sodium chloride, 6 mM sodium hydrogen phosphate, 4 mM sodium dihydrogen phosphate, 2 mM EDTA, 50 mM sodium fluoride, 1 mM sodium orthovanadate, 1 mM dithiothreitol, and 1 mM phenylmethane sulfonyl fluoride. The protein lysates were subjected to sodium dodecyl sulfate-polyacrylamide gel electrophoresis and transferred to polyvinylidene difluoride membranes (#IPVH00010, Millipore). The protein-bound membranes were blocked with 5% skim milk, washed, and incubated with the indicated primary antibodies. Several antibodies were diluted using a SignalBoost Immunoreaction Enhancer Kit (#407207; Millipore) to amplify the antibody reaction. Membranes were subsequently incubated with HRP peroxidase-conjugated secondary antibodies (Jackson ImmunoResearch Laboratories). Protein signals were developed using enhanced chemiluminescence reagents (#1705061; Bio-Rad) and a Fusion Solo S imaging system (VILBER, Collegien, France). Band density was measured using Evolution Capt software.

3-(4,5-Dimethylthiazol-2-yl)−2,5-diphenyl-2H-tetrazolium bromide (MTT) assay

Cell survival rates were quantified using an MTT assay (#MC1029-001–02; Biosesang, Gyeonggi-do, South Korea). Approximately 5×10^3 cells/well were seeded into 96-well culture plates. After incubation, each sample was treated with 500 μg/mL of MTT solution in RPMI or DMEM and further incubated for 2 h at 37 °C. Then, the RPMI medium, including MTT, was removed, and the intracellular purple formazan formed by MTT was solubilized by treatment with dimethyl sulfoxide (DMSO; #DMS555-1; Biopure, Ontario, Canada). The solubilized samples were then analyzed at 570 nm using an Epoch spectrophotometer (BioTek Instruments, Winooski, VT, USA).

Flow cytometry for apoptosis analysis

For apoptosis analysis, cells were trypsinized and stained with Annexin V-FITC using the ApoScreen Annexin V Apoptosis Kit-FITC (#10010-02; Southern Biotech, Birmingham, AL, USA) and 7-AAD (#402404; BioLegend, San Diego, CA, USA), according to the manufacturer's instructions. The stained cells were analyzed using a BD Accuri C6 flow cytometer (BD Biosciences, San Jose, CA, USA) and BD Accuri C6 Plus software (BD Biosciences). The percentage of total apoptotic cells was determined as the sum of the percentage of Annexin V^+/7-AAD^- (early apoptotic) cells and Annexin V^+/7-AAD^+ (late apoptotic) cells. Additionally, the percentage of living cells was determined using Annexin V^-/7-AAD^- cells.

Generation of *ATAT1* KD and overexpression cell lines

Stable cell lines were generated using the lentiviral vectors. The shRNA- or CDS-cloned constructs were packaged by cotransfection with pMD2.G (#12259; Addgene) and psPAX2 (#12260, Addgene) into HEK293T cells. Lentiviral particles were harvested from HEK293T cells after 72 h and used to infect target cells using 8 μg/mL polybrene. To establish stable cell lines, cells infected with lentiviruses containing shRNA were selected with 1 μg/mL puromycin. In contrast, cells infected with lentivirus containing CDS-cloned constructs were selected with 10 μg/mL blasticidin.

Live cell imaging

For live imaging experiments, cells were seeded into each well of six-well glass-bottom plates coated with 50 μg/mL rat tail type I collagen and incubated for 24 h post-transfection with plasmids (EB1-GFP for observing microtubule dynamics, and Mito-GCaMP6f and ER-GCaMP6f 150 for observing Ca^{2+} signal). Next, the cells were treated with or without drugs in FBS-containing growth media in a 5% CO_2 chamber at 37 °C. To observe microtubule dynamics, we captured images at 2 s intervals for 30 s using a Nikon ECLIPSE Ti2 inverted microscope system (Nikon, Tokyo, Japan) equipped with a digital camera, DS-Qi2 (Nikon), for live-cell imaging analysis. Microtubule growth rates were assessed by tracking each EB1-GFP comet and measuring its path speed over time using the advanced microscope software NIS-Elements Advanced Research (Nikon).

For observing the Ca^{2+} signal, cells were washed twice with Hank's buffered salt solution (HBSS, #NB203-04; WelGENE) and stimulated with ATP (PerkinElmer) and ionomycin (Invitrogen). Images were captured at 200 ms intervals for 5 min using the microscope and digital camera setup described above. The Ca^{2+} signal in the images was analyzed using the Register ROI plugin (ImageJ) and a time-series analyzer (v3.0).

Immunocytochemistry

Cells were seeded onto 12 mm coverslips coated with 50 μg/mL collagen at a density of approximately 2×10^4 cells/well. After incubation, the cells were fixed with cold methanol for 10 min and permeabilized with 0.5% Triton X-100 in PBS for an additional 10 min. Subsequently, the samples were blocked with 2% BSA and 1% glycine in PBS containing 0.1% Triton X-100 for 1 h. The resulting samples were stained with primary antibodies for 1 h at 22 °C and then incubated with fluorescein-conjugated secondary antibodies for 1 h at 22 °C after washing with 0.1% Triton X-100 in PBS. After staining, samples were mounted using Fluoromount-G (Southern Biotech). Cells were observed using an Eclipse 80i fluorescence microscope (Nikon), and images were captured using a digital camera, DS-Qi2 (Nikon). To quantitatively analyze the perinuclear Mito index and Mito-GCaMP6f signal, we adopted the methods described by [26] and [27], respectively. Images were processed using advanced microscope software NIS-Elements Advanced Research (Nikon) and Photoshop (Adobe Systems, San Jose, CA, USA).

Field-emission transmission electron microscopy

Cells were fixed with 2% glutaraldehyde (#G6257; Sigma-Aldrich) and 2% paraformaldehyde (#G6148; Sigma-Aldrich) in 0.05 M sodium cacodylate (#C0250; Sigma-Aldrich) buffer for 2 h at 22 °C and incubated for 16 h at 4 °C. The samples were washed with 0.05 M sodium cacodylate buffer and incubated in 1% osmium tetroxide diluted in 0.1 M sodium cacodylate buffer for 1 h at 4 °C. The samples were stained with 0.5% uranyl acetate for 16 h at 4 °C after washing with distilled water three times. Next, the samples were dehydrated with 30%, 50%, 70%, 80%, 90%, and 100% ethanol and embedded in Spur's resin. The samples were sectioned using an ultramicrotome. The samples were stained with uranyl acetate. The images were obtained using a JEM-F200 transmission electron microscope (JEOL, Tokyo, Japan).

RNA sequencing and bioinformatics analysis

Total RNA was extracted from MDA-231 WT, *ATAT1* knockout (KO), and eribulin-resistant cell lines. RNA quality and quantity were measured using an Agilent 2100 Bioanalyzer (Agilent Technologies, Amstelveen, The Netherlands) and Nanodrop ND-2000 (Thermo Scientific), respectively. To test and control RNA, we constructed a library using Quant-seq 3′ mRNA-Seq Library Prep Kit (Lexogen,

Vienna, Austria), according to the manufacturer's instructions as previously described [6, 28]. Single-end 75 RNA sequencing was performed using NextSeq 500 (Illumina, San Diego, CA, USA) at Ebiogen Inc. (Seoul, Korea). Functional annotation analysis was performed using the Database for Annotation, Visualization and Integrated Discovery (DAVID, https://david.ncifcrf.gov). Gene ontology (GO) analysis was performed using the ExDEGA GraphicPlus and Revigo software (http://revigo.irb.hr/). Kyoto Encyclopedia of Genes and Genomes (KEGG) pathway analysis was performed using ShinyGO 0.77 (http://bioinformatics.sdstate.edu/go/) software. The expression profile was obtained from the Gene Expression Omnibus (GEO, https://www.ncbi.nlm.nih.gov/geo/). Accession number GSE50811 was used for the GEO analysis.

Three-dimensional (3D) invasion assay

To generate tumor spheroids, 5×10^3 cells were seeded in 96-well ultralow attachment plates (SPL 3D™ Cell Floater, SPL Life Sciences, Gyeonggi-do, Korea, #39724) and incubated with culture media supplemented with 10% FBS for 24 h. Following incubation, the tumor spheroids were coated with a 200 µg/mL growth factor-reduced Matrigel solution for 24 h. As previously described, the tumor spheroids were mixed with 1 mg/mL rat tail type I collagen solution and polymerized for 1 h in a 37 °C incubator [29]. The tumor spheroids embedded within the 3D collagen matrix were then incubated under the specified conditions for 72 h. To analyze the survival of invasive cells under each condition, we stained the tumor spheroids using the Live/Dead™ Viability/Cytotoxicity Kit (Invitrogen, #L3224) following the manufacturer's instructions. Images were captured using a digital camera (DS-Qi2, Nikon), and cell invasiveness was determined by subtracting the area of invading spheroids from the initial spheroid area using NIS-Elements image analysis software (Nikon).

Live/dead assay

The Live/Dead™ Viability/Cytotoxicity Kit for mammalian cells (#L3224; Invitrogen) was used to evaluate cell viability. Cells seeded onto 12 mm coverslips coated with 50 µg/mL collagen were incubated with 1 µM Calcein-AM and 4 µM EthD-1 for 30 min at 37 °C. After incubation, PBS solution was added to clean the glass slides, and the coverslips were mounted on the glass slides. Images were obtained using an Eclipse 80i fluorescence microscope (Nikon) and captured using a digital camera, DS-Qi2 (Nikon). Images were processed using advanced microscope software NIS-Elements Advanced Research (Nikon, Tokyo, Japan).

Terminal deoxynucleotidyl transferase dUTP nick end labeling (TUNEL) assay

TUNEL assay was performed to detect apoptotic cells using DeadEnd™ Fluorometric TUNEL System (Promega, Madison, WI, USA) following the manufacturer's instructions.

In vivo xenograft

MDA-231 parental and EriR cells (1.5×10^7) were resuspended in 100 µL of RPMI 1640 without serum admixed with 100 µL Matrigel (#356231; Corning, NY, USA) and injected subcutaneously into six-week-old BALB/c-nude mice (Nara Biotech Co.). Tumor size was measured using calipers every 2 d, and the volume was calculated using the formula $L \times W^2 \times 0.5$, where L and W represent the tumor length and width, respectively. When the average tumor volume reached approximately 150 mm^3, the mice were treated with 0.1 mg/kg eribulin every 2 d through intravenous injection (i.v.) for 14 d and 0.5 mg/kg tubacin every day through intraperitoneal injection (i.p.) or 2 mg/kg CCT020312 every four days through i.p. for 26 d. The tumors were dissected and weighed at the endpoint. The experimental procedures were approved by the Institutional Animal Care and Use Committee of Chung-Ang University (Approval ID: 2019-00133).

Immunohistochemistry (IHC)

Tumors were fixed in 10% neutral buffered formalin (#010–1406-1010; GD CHEM, Chuncheongbuk-do, South Korea) and embedded in paraffin blocks. Sectioned tumors were blocked with an M.O.M™ blocking solution. Sectioned tumors were stained with specific antibodies for acetyl-α-tubulin and cytochrome c. Nuclei were counterstained with DAPI. Sectioned tumors were mounted using Fluoromount-G. Fluorescence-positive cells (%) were analyzed using NIS-Elements advanced imaging software (Nikon).

RNA isolation and quantitative reverse transcription PCR (qRT-PCR)

Total RNA was isolated using RNAiso Plus reagent (#9109; TaKaRa, Tokyo, Japan) following manufacturer's instructions. For synthesis of complementary DNA, a total 1 µg of RNA was taken with 100 mM oligo primers and PrimeScript reverse transcriptase (#2680; TaKaRa). qRT-PCR was performed with SYBR Premix Ex-Taq II (#RR820; TaKaRa) using QuantStudio 3 (Applied Biosystems, city, CA, USA). The primers used for qRT-PCR are as follows: *ATAT1* (forward: 5′-TTTGCATCCTGGACTTTT-3′, reverse: 5′-TTG TTCACCTGTGGGACT-3′), *HDAC6* (forward: 5′-AAG TAGGCAGAACCCCCAGT-3′, reverse: 5′-GTGCTTCAG

CCTCAAGGTTC-3′), and *GAPDH* (forward: 5′-GACCCC TTCATTGACCTC-3′, reverse: 5′-TCCTGGAAGATGGTG ATG-3′).

Statistical analysis

Statistical analyses were performed using GraphPad Prism 8.0 (GraphPad Software, San Diego, CA, USA). The significance of differences between data was examined using Student's unpaired t-test to compare two groups and one-way analysis of variance (one-way ANOVA) or two-way ANOVA to compare more than two groups. Data are presented as mean ± standard deviation (S.D.) from two or three independent experiments. Tukey's multiple comparison test was performed as a post-hoc test for all one-way ANOVA or two-way ANOVA. One-way ANOVA F values are presented in the figure legends as $F_{(DFn, DFd),}$ where DFn is the df numerator and DFd is the df denominator. *p*-values less than 0.05 were considered statistically significant ($*p < 0.05$, $**p < 0.01$, $***p < 0.001$, and $****p < 0.0001$).

Results

Reduced microtubule acetylation increases eribulin resistance in breast cancer cells

We investigated the effect of eribulin, a microtubule-targeting agent, on tubulin PTMs in TNBC cell lines by treating them with eribulin at its half-maximal inhibitory concentration (IC_{50}). Specifically, MDA-231 cells were treated with eribulin at 1.2 nM (50% of IC_{50}) and 2.4 nM (IC_{50}), which resulted in approximately 60% and 50% cell viability, respectively. Similarly, in Hs578T cells, eribulin treatment also reduced cell viability in a dose-dependent manner, with approximately 50% viability at its IC_{50} concentration (1 nM) (Fig. 1A). Eribulin is a microtubule dynamics inhibitor that is known to induce mitotic arrest, which disrupts chromosome alignment and leads to G2/M phase cell cycle arrest [30, 31]. Our results also revealed that eribulin considerably reduced microtubule dynamics, leading to chromosomal misalignment and cell cycle arrest (Fig. S1A–D). Although tubulin PTMs, including microtubule acetylation, detyrosination, and delta2 modification are predominantly found in stable microtubules [32], our results indicated that eribulin treatment specifically increased microtubule acetylation but not detyrosination and delta2 modification (Figs. 1B, S1E). The increase in microtubule acetylation was particularly noticeable around the nucleus (Fig. 1C).

To investigate whether the increase in microtubule acetylation contributes to eribulin-induced cell death, we utilized a lentiviral shRNA system to downregulate *ATAT1*, the gene encoding microtubule acetyltransferase (α-TAT1). We evaluated eribulin sensitivity in *ATAT1* KD cell lines (Fig. 1D). Unlike Mock (control) cells, *ATAT1* KD cells exposed to eribulin did not show increased microtubule acetylation or decreased microtubule dynamics (Fig. S2A, B). Furthermore, in Mock cells, apoptotic markers, such as cleaved caspase 9, cleaved PARP, and CHOP increased in correlation with eribulin concentration (Fig. 1E). However, *ATAT1* KD cells demonstrated reduced sensitivity to eribulin-induced cell death, as evidenced by a decrease in apoptotic markers and an increase in cell viability following eribulin treatment (Fig. 1E, F). To validate these results, we generated *ATAT1* KO cell line using the CRISPR/Cas9 system. These *ATAT1* KO cells did not enhance microtubule acetylation upon eribulin treatment and also displayed resistance to eribulin (Fig. S2C–E). These results highlight the crucial role of microtubule acetylation in mediating eribulin-induced cell death in breast cancer cells.

To investigate whether breast cancer cells develop resistance to eribulin via reduced microtubule acetylation, we generated EriR cells through six-month exposure to eribulin. The resulting EriR cells derived from MDA-231 and Hs578T cells displayed a significant increase in their IC_{50} values for eribulin by approximately 21- and 28-fold, respectively (Fig. 1G). When treated with eribulin, the EriR cells exhibited neither suppressed growth nor decreased microtubule dynamics (Fig. S2F, G). Using a 3D spheroid invasion assay, we found that the EriR cells displayed increased invasiveness compared to their parental counterparts (Video S1). Notably, the levels of microtubule acetylation in EriR cells were substantially lower than those in the parental cells. Furthermore, unlike in parental cells, eribulin had minimal effect on microtubule acetylation levels in EriR cells (Fig. 1H). Collectively, our findings suggest that decreased microtubule acetylation may contribute to developing eribulin resistance in breast cancer cells.

Eribulin-driven microtubule acetylation enhances mitochondrial Ca^{2+} absorption

Excessive Ca^{2+} flux at ER-mitochondria contact sites, especially along acetylated microtubules, often results in cell death [5, 20]. To investigate the effect of microtubule acetylation on ER-mitochondria contacts in response to eribulin treatment, we first measured the distance between the ER and mitochondria using field-emission transmission electron microscopy (FE-TEM) in both Mock and *ATAT1* KD cells. Notably, the gap between the ER and mitochondria was wider in *ATAT1* KD cells compared to that in Mock (control) cells (Fig. 2A), suggesting that microtubule acetylation is required for ER-mitochondria contact.

Subsequently, we examined whether eribulin induces ER-mitochondria contacts. Cells were treated with eribulin and we measured the distance between the ER and mitochondria

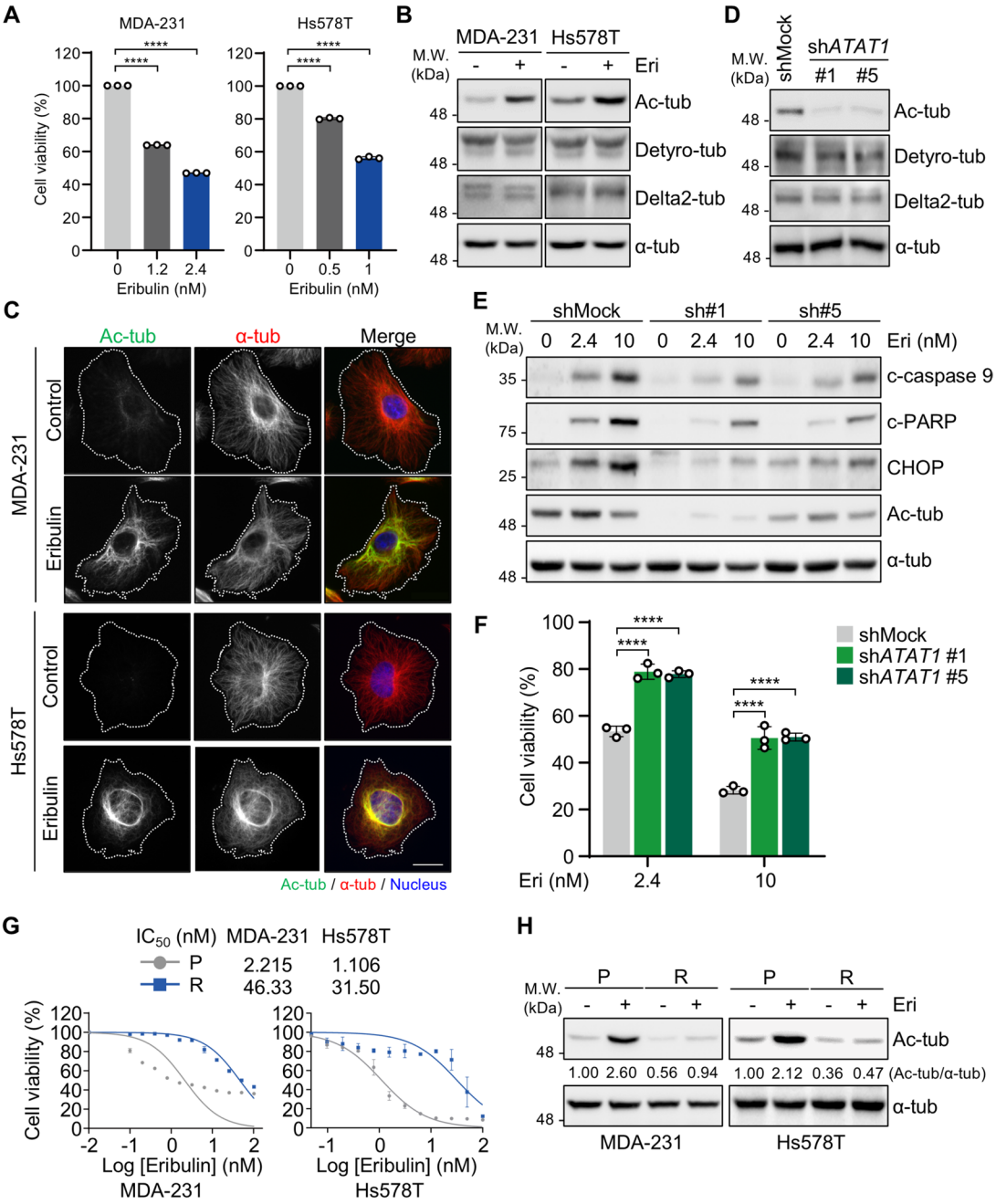

Fig. 1 Microtubule acetylation is required for eribulin-induced cell death in breast cancer cells. **A** MDA-MB-231 (MDA-231) and Hs578T cells were treated with eribulin as indicated for 72 h. MTT assay was performed to measure the viability of cells. Statistical analysis was performed using one-way ANOVA with Tukey's multiple comparisons. One-way ANOVA, $F_{2,\ 6}=217{,}442$, $F_{2,\ 6}=4302$. **B** MDA-231 and Hs578T cells were incubated with or without 2.4 nM and 1 nM eribulin, respectively, for 24 h. Cell lysates were applied to western blotting with Ac-tub, detyro-tub, delta2-tub, and α-tub antibodies. **C** Immunofluorescence analysis with Ac-tub (green), α-tub (red), and nucleus (blue) in MDA-231 and Hs578T cells treated with or without eribulin 2.4 nM and 1 nM, respectively, for 24 h. Scale bar, 20 µm. **D** Decreased expression of *ATAT1* in MDA-231 cells was verified by western blotting. Cell lysates were applied to western blotting with Ac-tub, detyro-tub, delta2-tub, and α-tub antibodies. **E** shMock and sh*ATAT1* #1, #5 MDA-231 cells were treated with eribulin as indicated for 72 h. Cell lysates were applied to western blotting with cleaved caspase 9 (c-caspase 9), cleaved PARP (c-PARP), CHOP, Ac-tub, and α-tub antibodies. **F** MDA-231 shMock and sh*ATAT1* #1, #5 cells were treated with eribulin 2.4 nM and 10 nM for 72 h. MTT assay was performed to measure the viability of cells. One-way ANOVA $F_{5,\ 12}=141.8$. **G** Cell viability curves of MDA-231 and Hs578T parental (P) and eribulin-resistant (R) cells after eribulin treatment for 72 h. MTT assay was performed to measure the viability rate of cells. **H** MDA-231 and Hs578T P and R cells were incubated with eribulin (MDA-231, 2.4 nM; Hs578T, 1 nM, 24 h). The mean levels of Ac-tub from three independent experiments, shown below the blots, were normalized to α-tub. ****$p<0.0001$

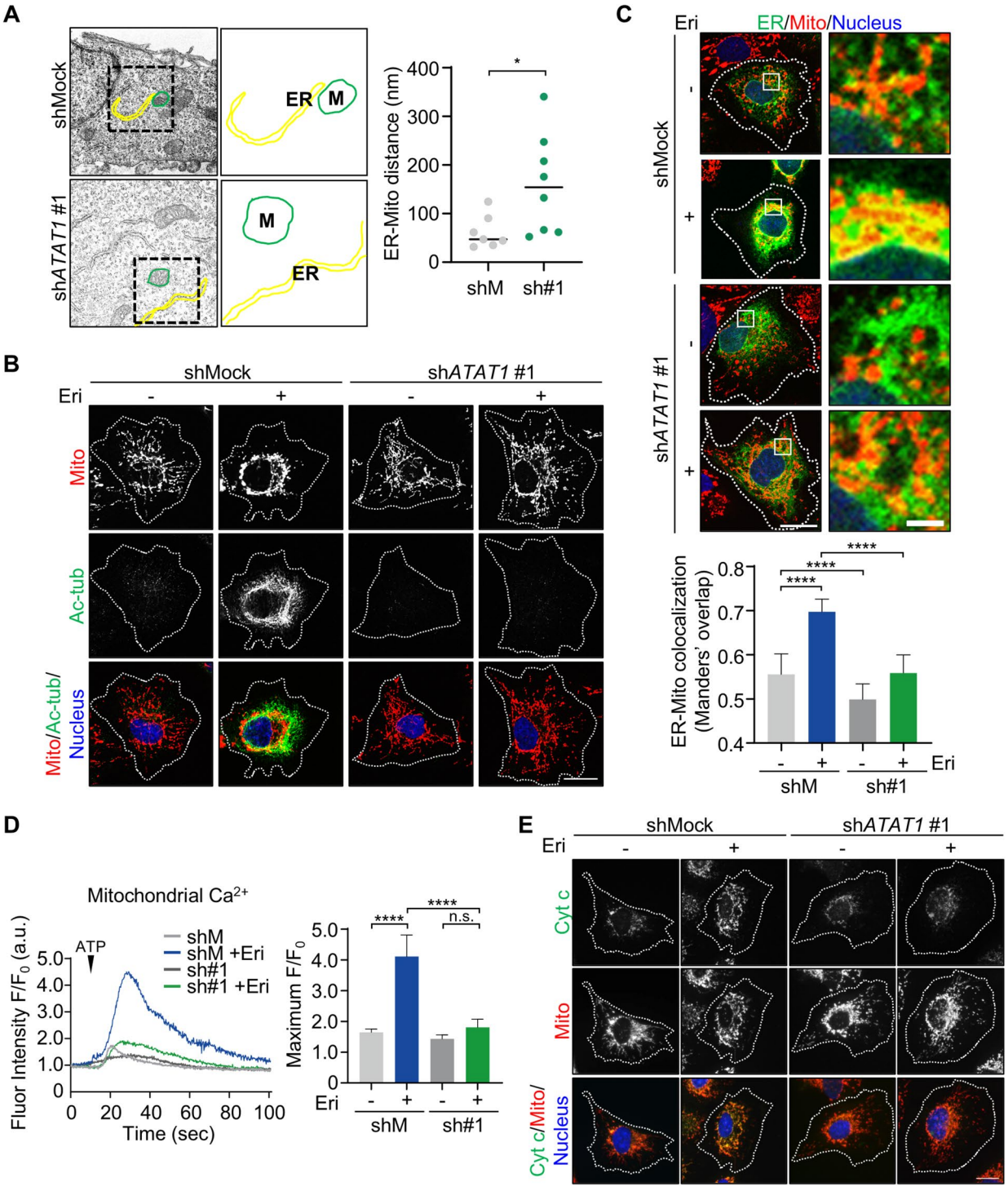

through FE-TEM images. The results showed that the ER and mitochondria become physically closer upon eribulin treatment (Fig. S3A). To further investigate whether ER-mitochondria contacts are modulated in a microtubule acetylation-dependent manner rather than solely by microtubules dynamics, we treated sh*ATAT1* cells with eribulin at 2.4 nM (IC_{50} for shMock cells) and 10 nM (IC_{50} for sh*ATAT1* cells) (Fig. 1F). Treatment with both 2.4 nM and 10 nM eribulin in sh*ATAT1* cells significantly increased the percentage of misaligned chromosomes due to disruption of spindle structures (Fig. S4A). However, despite these changes in spindle dynamics, ER-mitochondria contacts remained unchanged in sh*ATAT1* cells under both conditions (Fig. S4B). These results demonstrate that ER-mitochondria contacts are

◂**Fig. 2** Ca^{2+} transfer from ER to mitochondria is promoted by eribulin-induced microtubule acetylation. **A** Field-emission transmission electron microscopy images of MDA-MB-231 (MDA-231) shMock and sh*ATAT1* #1 cells (left images). The images show the endoplasmic reticulum (ER, yellow line) and mitochondria (M, green line; right images). The scattered plot shows the distance of ER-mitochondria in shMock and sh*ATAT1* #1. Scale bar, 500 nm. Data are presented as the mean ± standard deviation. Statistical analysis was performed using the Student's unpaired t-test. **B** Immunofluorescence analysis using confocal microscopy with mitochondria (mito, red; stained with MitoTracker Red CMXRos dye), Ac-tub (green), and nucleus (blue) in shMock and sh*ATAT1* #1 Hs578T cells with indicated drugs (eribulin 1 nM, 24 h). Scale bar, 20 μm. **C** Immunofluorescence analysis using confocal microscopy with mitochondria (mito, red; stained with MitoTracker Red CMXRos dye) and nucleus (blue) in shMock and sh*ATAT1* #1 Hs578T cells transfected with GFP-SEC61β (ER) with or without 1 nM eribulin treatment for 48 h (left images). The images to the right show the enlarged images from the boxed regions. The bar graph shows the Manders' overlap coefficient between ER and mitochondria in shMock and sh*ATAT1* #1 cells (n = 21, each group). Scale bar, 20 μm (left images) and 2.5 μm (right images). Statistical analysis was performed using one-way ANOVA with Tukey's multiple comparisons. One-way ANOVA, $F_{3, 80} = 101.6$. **D** Relative fluorescence intensity (y-axis) is measured over time (x-axis) of shMock and sh*ATAT1* #1 Hs578T transfected with mitochondrial Ca^{2+} indicator Mito-GCaMP6f. Cells were treated with 1 nM eribulin for 48 h and stimulated with 50 μM ATP at 10 s (arrowhead). The bar graph shows the peak of fluorescence intensity. One-way ANOVA $F_{3, 15} = 51.19$. **E** Immunofluorescence analysis with cytochrome c (Cyt c, green), mitochondria (mito, red; stained with MitoTracker Red CMXRos dye), and nucleus (blue) in shMock and sh*ATAT1* #1 Hs578T cells treated with or without eribulin 1 nM for 72 h. Scale bar, 20 μm. $*p < 0.05$, $****p < 0.0001$, n.s. not significant

specifically regulated by eribulin-induced microtubule acetylation rather than microtubule dynamics alone. Furthermore, the reduction of these contacts in sh*ATAT1* cells may contribute to eribulin resistance.

We also found that mitochondria are markedly accumulated around the nucleus, reflecting the spatial pattern of eribulin-induced microtubule acetylation (Fig. S3B). Eribulin treatment also increased spatial overlap between the ER and mitochondria around nucleus, as quantified by Mander's overlap index (Fig. S3C). Additionally, we used genetically encoded reporters for mitochondrial and ER proteins, respectively, along with split GFP (spGFP) reporter to label the ER-mitochondria contact sites [33]. This allows us to evaluate the effect of eribulin on ER-mitochondria contacts. Our results confirmed that eribulin treatment significantly increased the size of GFP-positive puncta, particularly in regions where mitochondria are densely packed around the nucleus (Fig. S3D).

To monitor the changes in mitochondrial Ca^{2+} concentrations resulting from altered ER-mitochondrial contacts, we introduced the mitochondrial Ca^{2+} indicator, Mito-GCaMP6f, and recorded its fluorescence over time. Eribulin-treated cells exhibited a significant increase in mitochondrial Ca^{2+} levels upon ATP stimulation, accompanied by increased cytochrome c levels (Fig. S3E, F; Video S2). To verify whether eribulin treatment causes abnormal ER Ca^{2+} storage, we measured the saturation fluorescence signal of ER Ca^{2+} stimulated by ionomycin using the ER Ca^{2+} indicator, ER-GCaMP6-150 [34]. Consequently, eribulin-treated cells showed similar levels of ER Ca^{2+} compared to untreated cells, indicating that the eribulin-induced augmented mitochondrial Ca^{2+} levels were not due to impaired ER Ca^{2+} storage (Fig. S3G).

In contrast, *ATAT1* KD cells did not exhibit eribulin-induced clustering of mitochondria near the nucleus (Figs. 2B, S5A). Following eribulin treatment, these *ATAT1* KD cells also showed fewer ER-mitochondrial contacts than Mock cells (control) (Figs. 2C, S5B), resulting in reduced mitochondrial Ca^{2+} uptake and cytochrome c levels in the cytosol (Fig. 2D, E). Overall, our findings suggest that eribulin-induced microtubule acetylation promotes Ca^{2+} transfer to the mitochondria, thereby contributing to cellular death.

Increasing microtubule acetylation levels are not sufficient to counteract eribulin resistance

In EriR cells, which have reduced microtubule acetylation, ATP-stimulated mitochondrial Ca^{2+} levels remained largely unchanged after eribulin treatment (Fig. 3A). This observation aligns with our previous observations that highlighted abnormal Ca^{2+} transfer in eribulin-treated cells with induced microtubule acetylation, but not in *ATAT1* KD cells (Fig. 2D). Based on these insights, we investigated whether enhanced microtubule acetylation counteracts eribulin resistance. We generated an *ATAT1*-overexpressed EriR cell line (Fig. 3B). These modified EriR cells exhibited notable perinuclear mitochondrial clustering compared to original EriR cells (Fig. S6A). Additionally, the overlap between the ER and mitochondria in *ATAT1*-overexpressing EriR cells exceeded that observed in EriR cells (Figs. 3C, S6B). Upon evaluating the effect of eribulin on mitochondrial Ca^{2+} levels in *ATAT1*-overexpressed EriR cells, the Mito-GCaMP6f signal intensity, normalized against the MitoTracker signal to indicate mitochondrial mass, remained largely constant, irrespective of eribulin treatment (Fig. 3D). Moreover, the cytochrome c levels did not change in eribulin-treated *ATAT1*-overexpressed EriR cells (Fig. 3E). Importantly, enhanced microtubule acetylation in EriR cells did not increase their sensitivity to eribulin (Fig. 3F). In addition, increasing microtubule acetylation levels by silencing of histone deacetylase 6 (HDAC6) in EriR cells also did not overcome eribulin resistance (Fig. S6C, D). These results suggest that while microtubule acetylation is important for ER-mitochondria contact, it is not the sole determinant of eribulin-induced abnormal mitochondria Ca^{2+} level in mitochondria and cell death.

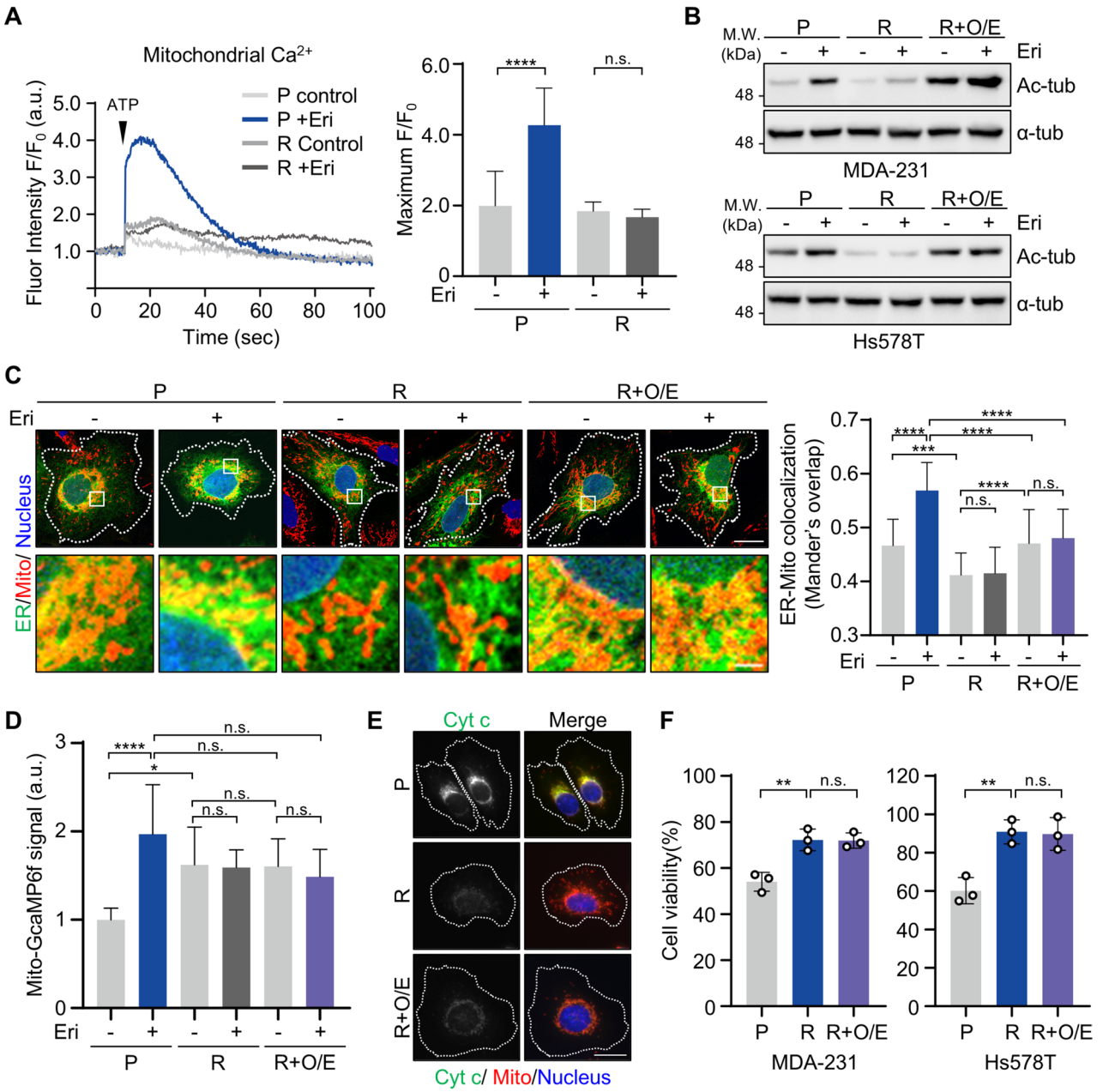

Fig. 3 Upregulation of microtubule acetylation in eribulin-resistant (EriR) cells does not overcome eribulin resistance. **A** Relative fluorescence intensity is measured over time of Hs578T parental (P), and eribulin-resistant (R) cells transfected with mitochondrial Ca^{2+} indicator Mito-GCaMP6f. Cells treated with 1 nM eribulin for 48 h and stimulated with 50 μM ATP at 10 s (arrowhead). The bar graph shows the peak of fluorescence intensity. Statistical analysis was performed using one-way ANOVA with Tukey's multiple comparisons. One-way ANOVA, $F_{3,\ 34} = 18.84$. **B** MDA-MB-231 (MDA-231) and Hs578T P, R, and *ATAT1*-overexpressed R (R + O/E) cells were incubated with or without eribulin (MDA-231, 2.4 nM; Hs578T, 1 nM, 24 h). Cell lysates were applied to western blotting with Ac-tub and α-tub antibodies. **C** Immunofluorescence analysis using confocal microscopy with mitochondria (mito, red; stained with MitoTracker Red CMXRos dye) and nucleus (blue) in Hs578T P, R, and R + O/E cells transfected with GFP-SEC61β (ER) with 1 nM eribulin treatment for 48 h (upper images). Lower images show the enlarged images. The bar graph shows the Mander's overlap coefficient between ER and mitochondria in Hs578T P, R, and R + O/E cells with eribulin 1 nM for 48 h (n = 35, each group). One-way ANOVA, $F_{5,\ 204} = 42.87$. Scale bar, 20 μm (upper images) and 2.5 μm (lower images). **D** The bar graph shows the intensity of Mito-GCaMP6f normalized to Mitotracker intensity in Hs578T P, R, and R + O/E cells transfected with Mito-GCaMP6f with eribulin treatment (1 nM, 48 h). One-way ANOVA, $F_{5,\ 42} = 6.332$. **E** Immunofluorescence analysis with cytochrome c (Cyt c, green), mitochondria (mito, red; stained with MitoTracker Red CMXRos dye), and nucleus (blue) in Hs578T P, R, and R + O/E cells upon eribulin treatment (1 nM, 72 h). Scale bar, 20 μm. **F** MDA-231 and Hs578T P, R, and R + O/E cells were treated with eribulin for 72 h (MDA-231, 2.4 nM; Hs578T, 1 nM). MTT assay was performed to measure the viability of cells. One-way ANOVA, $F_{2,\ 6} = 19.57$, $F_{2,\ 6} = 17.12$. $^{*}p < 0.05$, $^{**}p < 0.01$, $^{***}p < 0.001$, $^{****}p < 0.0001$, n.s. not significant

PERK signaling plays a pivotal role in eribulin-induced cell death

To investigate the molecular pathways potentially associated with eribulin resistance, RNA sequencing (RNA-seq) was performed to compare MDA-231 parental cells with EriR cells. The analysis revealed 3165 differentially expressed genes (DEGs) in EriR cells, with 1521 genes upregulated and 1644 genes downregulated (Figs. 4A, S7A). We initially focused on functional annotation and GO analysis of the downregulated genes in EriR cells, highlighting their association with ER and mitochondria (Fig. 4B). Moreover, GO analysis revealed that these downregulated genes primarily functioned in responses to ER stress (GO:0034976) and inhibition of apoptosis (GO:0043066) (Fig. 4C).

ER stress can induce notable changes in the ER morphology [35]. Therefore, we initially analyzed the morphological changes of the ER upon eribulin treatment using FE-TEM. Eribulin-treated cells exhibited shorter tubular ER lengths and thicker ER lumen width compared to untreated cells (Fig. S3A). Cells with denser ER networks or enhanced sheet-like ER morphology have been reported to have an increased ER lumen width and this width is enhanced under ER stress conditions [6, 36, 37]. Collectively, we confirmed that eribulin treatment elevated the ER stress by observing these abnormal alterations of ER morphology. However, super-resolution microscopy revealed abnormal ER morphology in the parental cell yet was barely observed in EriR cells upon eribulin treatment (Fig. S7B).

We identified 151 genes downregulated in EriR cells that overlapped with 1,221 genes upregulated after eribulin treatment, according to data from the public GEO database (GSE50811) (Fig. 4D). Subsequent GO analysis of these 151 genes revealed a significant association with ER stress-related processes, as shown in Fig. 4E. Notably, the PERK and IRE1α signaling pathways, which are branches of the UPR signaling, have been implicated in maintaining ER Ca^{2+} balance [25, 38, 39]. Eribulin treatment induced increased phosphorylation of both PERK and IRE1α in parental cells; however, this increase was notably absent in eribulin-treated EriR cells (Fig. 4F). To ascertain the exact signaling pathway responsible for eribulin-induced cell death, we silenced both PERK and IRE1α using a lentiviral shRNA system and subsequently assessed cell viability following eribulin treatment (Fig. 4G, H). As shown in Fig. 4H, specific suppression of PERK resulted in increased cell survival rates upon eribulin treatment. Moreover, in PERK-silenced cells treated with eribulin, microtubule acetylation and ER-mitochondria contacts increased, while mitochondrial Ca^{2+} levels were significantly reduced (Fig. S7C-E). These findings strongly suggest that activation of PERK signaling plays a crucial role in mediating eribulin-induced cell death.

Increased microtubule acetylation with activation of PERK enhances cell death in EriR cells

To explore whether PERK activation combined with microtubule acetylation can restore the cell death in EriR cells, we treated *ATAT1*-overexpressed EriR cells with the PERK activator, CCT020312 (CCT), at a concentration that did not affect the viability of EriR cells [40]. Initially, we assessed the physical interaction between the ER and mitochondria and observed that neither eribulin nor CCT treatment considerably altered the co-localization of the ER and mitochondria in *ATAT1*-overexpressed EriR cells, which already demonstrated increased overlap of these organelles compared to EriR cells (Figs. 5A, S6B, S8A). However, treatment with CCT increased mitochondrial Ca^{2+} levels and cytochrome c release, resulting in a notable reduction in the viability of *ATAT1*-overexpressed EriR cells with high microtubule acetylation levels (Fig. 5B–D). Similarly, the combination of eribulin and CCT led to elevated mitochondrial Ca^{2+} and cytochrome c levels, culminating in a significant reduction in the viability of *ATAT1*-overexpressed EriR cells (Fig. 5B–D).

In cancer treatment, predicting precise drug combinations to overcome drug resistance is vital for effective combination therapies [41]. Based on these results, we investigated whether inducing microtubule acetylation and PERK activity could be novel therapeutic strategies to induce cell death in EriR cells. To test this approach, we used CCT and tubacin, a HDAC6 inhibitor, in the absence of available drugs to directly activate α-TAT1 (Fig. S8B) [42, 43]. In EriR cells treated with CCT and tubacin together, we observed enhanced contact between the ER and mitochondria, along with significant increases in mitochondrial Ca^{2+} and cytochrome c levels (Figs. 5E–G, S8C). Moreover, although monotherapy with CCT or tubacin did not markedly affect cell viability, their combination synergistically promoted cell death (Figs. 5H, S8D, E). Additionally, we evaluated the cytotoxicity of combined therapy with tubacin and CCT in parental cells. The combination resulted in a significant reduction in cell viability in parental cells, similar to its effects in EriR cells (Fig. S8F). However, the combined treatment exerted stronger growth inhibition in EriR cells than in parental cells (cell viability after combined therapy: approximately 52.69% in parental cells and 39.76% in EriR cells, Fig. 5H), likely due to the lower baseline levels of microtubule acetylation and PERK activity in EriR cells.

Before assessing the therapeutic efficacy of combining CCT and tubacin in vivo, we generated 3D spheroids with EriR cells to mimic 3D tumor growth. We treated these spheroids with either CCT or tubacin. The results showed that while treatment with each drug alone did not change the proportion of dead cells within the spheroids or their invasive capabilities, the combination of CCT and

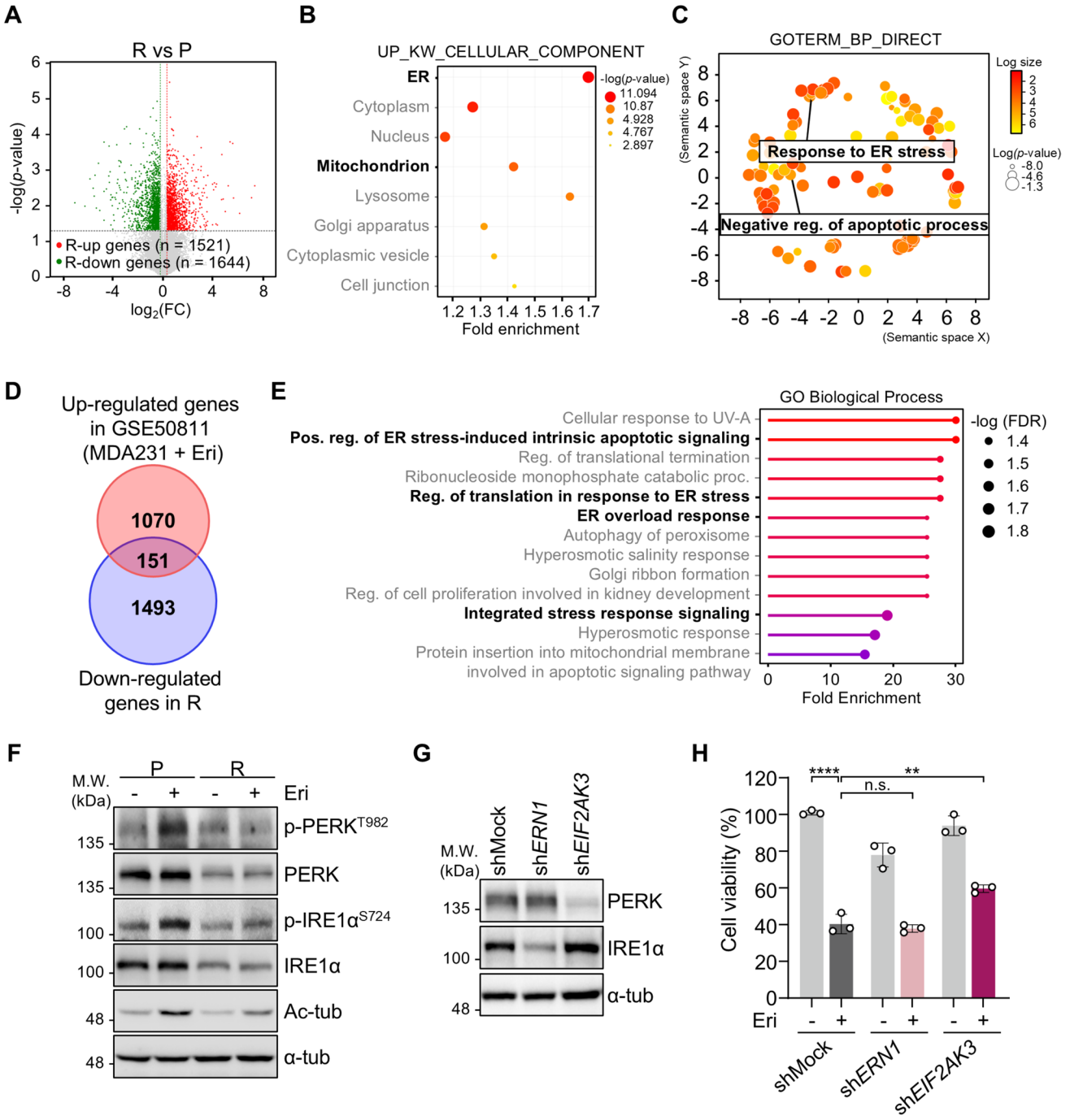

Fig. 4 Activation of PERK signaling is associated with eribulin resistance. **A** Volcano plot of differentially expressed genes (DEGs) in MDA-MB-231 (MDA-231) eribulin-resistant (R) cells compared to parental (P) cells based on RNA-sequencing (RNA-seq) datasets. Green dots represent significantly downregulated genes, and red dots represent significantly upregulated genes in MDA-231 R cells. **B** DAVID functional annotation of a cellular component in downregulated genes of R cells. **C** GO analysis of downregulated genes in MDA-231 R cells concerning their roles in biological processes was performed using DAVID gene ontology software. **D** Venn diagram shows overlapped genes among 1,644 downregulated genes in MDA-231 R cells and 1,221 upregulated genes in eribulin-treated MDA-231 cells obtained from gene expression datasets GSE50811. **E** GO analysis of 151 genes isolated in (D) was conducted to decipher their roles in biological processes using Shiny GO software **F** Hs578T P and R cells were incubated with or without eribulin 1 nM for 48 h. Cell lysates were applied to western blotting with p-PERK^{T982}, PERK, p-IRE1α^{S724}, IRE1α, Ac-tub, and α-tub antibodies. **G** Decreased expression of PERK and IRE1α in Hs578T cells was verified by western blotting. Cell lysates were applied to western blotting with PERK, IRE1α, and α-tub antibodies. **H** shMock, sh*ERN1*, and sh*EIF2AK3* Hs578T were treated with eribulin 1 nM for 72 h. MTT assay was performed to measure the viability of cells. Statistical analysis was performed using one-way ANOVA with Tukey's multiple comparisons. One-way ANOVA, $F_{5,\ 12} = 118.5$. $^{**}p < 0.01$, $^{****}p < 0.0001$, n.s. not significant

tubacin considerably increased the percentage of dead cells and notably reduced the invasive ability of the spheroids (Figs. 6A, S9). MDA-231 EriR tumor xenografts were established in BALB/c nude mice to evaluate the therapeutic benefits of CCT and tubacin combination treatment in vivo. We confirmed that the EriR tumor xenograft model maintained eribulin resistance in vivo, as indicated by the increased growth of EriR tumors compared to that of the parental tumors, which exhibited decreased tumor growth upon eribulin treatment with no changes in body weight (Fig. S10A, B).

Consistent with our in vitro observations, the combination of CCT and tubacin, unlike the treatments of each drug alone, more effectively inhibited tumor growth and reduced tumor weight compared to vehicle-only controls in the EriR xenograft model (Fig. 6B–D). IHC analysis of the dissected tumors at the study endpoint showed that the CCT and tubacin combination treatment increased the percentage of cells positive for microtubule acetylation and cytochrome c (Fig. 6E, F). Furthermore, the lack of observed changes in body weight suggested that this combination therapy was not significantly toxic (Fig. S10C). These findings suggest that increased microtubule acetylation and PERK activity induce structural and functional changes in the ER and mitochondria, leading to cell death in EriR cells. This highlights the potential of targeting microtubule acetylation and PERK activity as a therapeutic strategy for eradicating EriR cells.

Discussion

Microtubules are essential for various cellular functions, making them primary targets in anticancer drug development. However, drugs like eribulin, which targets microtubules, often cause severe side effects and the rapid onset of drug resistance. Our study highlights that microtubule acetylation plays a critical role in eribulin-mediated cell death. We found that eribulin-induced microtubule acetylation enhanced ER-mitochondria interactions, leading to mitochondrial Ca^{2+} overload and subsequent cell death. However, EriR cells showed reduced microtubule acetylation and efforts to restore it were insufficient to overcome this resistance. Further analysis revealed the importance of the ER stress response and PERK activity in mediating eribulin-induced cell death, the downregulation of PERK signaling and the lack of microtubule acetylation appeared to contribute to their resistance. While eribulin remains effective in treating metastatic breast cancer, resistance remains a significant challenge, highlighting the need for novel treatment strategies. Our findings suggest combining strategies to enhance microtubule acetylation and PERK activation may improve eribulin efficacy in resistant cells. By utilizing pharmacological agents or *ATAT1* overexpression to promote microtubule acetylation and activating PERK, we propose a potential therapeutic strategy to overcome resistance and induce cell death in eribulin-resistant cells.

Microtubule acetylation can be increased by various stressors, among which the ROS-induced increase is particularly notable. Under oxidative stress, H_2O_2 treatment activates AMP-activated protein kinase (AMPK), upregulating αTAT1/MEC-17 and enhancing microtubule acetylation [44]. However, combining eribulin with NAC, a ROS scavenger, did not decrease eribulin-induced microtubule acetylation or affect cell viability (data not shown). This suggests that neither ROS nor AMPK activation plays a role in a microtubule acetylation increase following eribulin treatment. Enzymatic regulation of microtubule acetylation involves αTAT1 as one acetyltransferase and HDAC6 and sirtuin 2 (SIRT2) as deacetylases [4]. We observed that eribulin treatment did not alter the expression of *ATAT1* and *HDAC6* (Fig. S11A). Paclitaxel, which binds to β-tubulin, increases microtubule acetylation levels, possibly by limiting HDAC6 accessibility due to conformational changes in the α-tubulin side chains [45]. Similarly, changes in the acetylation state of K40 in α-tubulin can later affect the accessibility of αTAT1 [46]. Stable microtubules are typically acetylated [47], and eribulin, which stabilizes microtubules by binding near the vinca domain of β-tubulin [48], reduces microtubule dynamics, as observed by the movement of the GFP-EB1 fluorescence signal (Fig. S1A, B). The binding of eribulin to the vinca domain or its inhibition of microtubule dynamics could modify enzyme accessibility. Although TGF-β-activated kinase 1 and casein kinase 2 are also known to regulate αTAT1 activity [49, 50], further investigation is needed to determine whether eribulin alters their activities.

Our findings revealed that eribulin treatment leads to an increased mitochondria accumulation around the nucleus, a phenomenon attenuated in *ATAT1* KD cells, suggesting the involvement of microtubule acetylation (Fig. 2B). Mitochondria use actin for short-range movement and microtubules for long-range transport. While actin-based movement is linked to the interaction between mitochondrial Rho GTPases 1/2 (Miro 1/2) in the OMM and myosin motor proteins, the exact mechanism remains unclear. In contrast, microtubule-driven transport is facilitated by two motor proteins: Miro/trafficking kinesin protein (TRAK)/kinesin complex drives anterograde transport, while the Miro/TRAK/dynactin/dynein complex handles retrograde transport [51, 52]. Previous studies suggest that microtubule acetylation enhances the binding affinity of kinesin and dynein to microtubules, with acetylated microtubules showing increased bundling and preferential recruitment of kinesin-1 [53]. Additionally, Trichostatin A, a tubulin deacetylase inhibitor, increases the binding of dynactin/dynein to acetylated microtubules [54]. The nuclear translocation of yes-associated protein by dynein is reduced in αTAT1 KO MEFs, further indicating

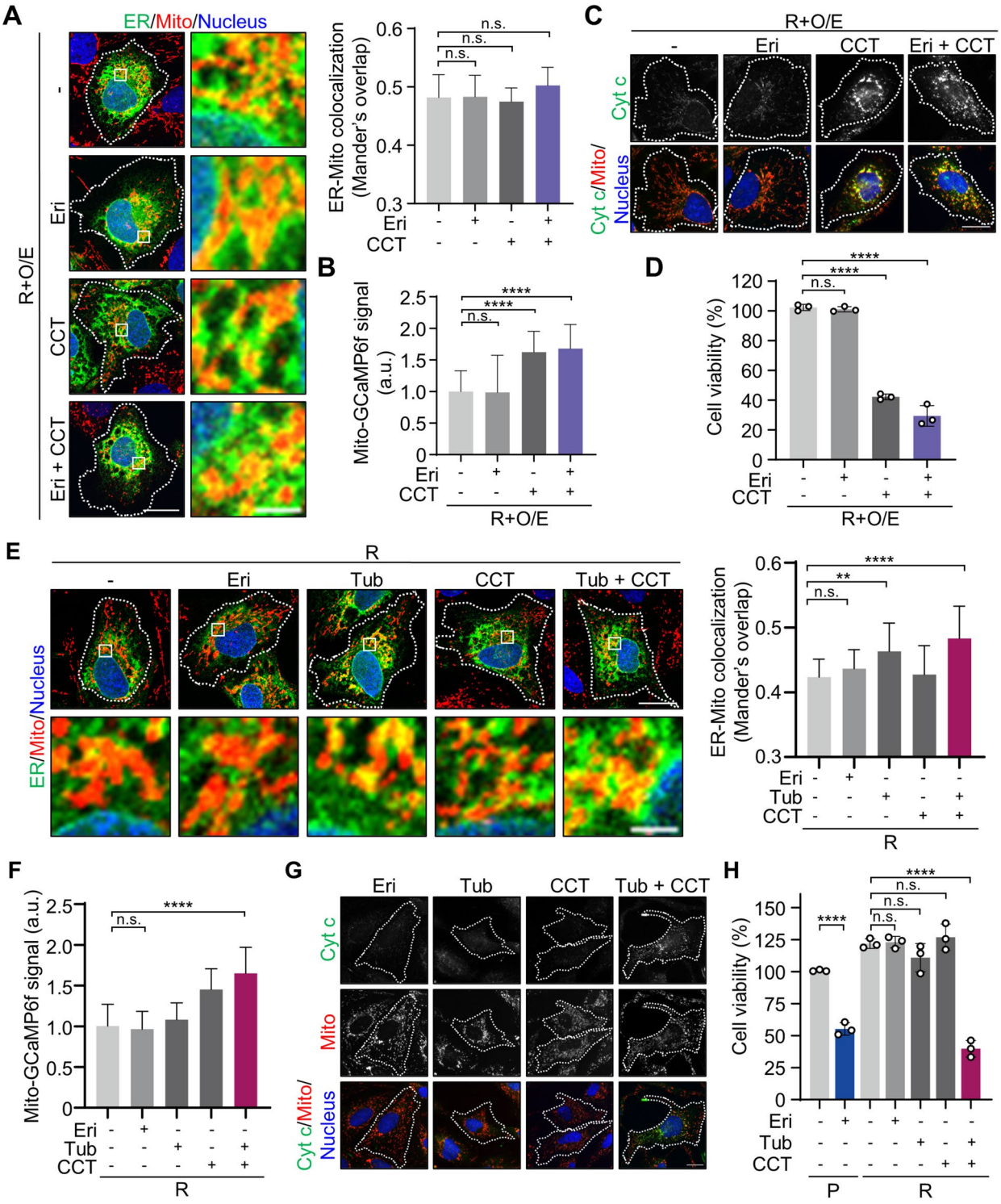

the role of microtubule acetylation in motor protein transport [28]. These observations suggest that mitochondrial clustering around the nucleus following eribulin treatment is likely driven by the preferential binding of motor proteins to the perinuclear acetylated microtubules. In addition, it has been reported that MFN2-dependent recruitment of α-TAT1 regulates the contact sites between acetylated microtubules and mitochondria, influencing mitochondrial transport and function [55]. Inhibition of MFN2 expression may disrupt this recruitment, potentially interfering with mitochondrial transport to acetylated microtubules and contributing to eribulin resistance by reducing ER-mitochondria contact. However, our RNA-seq data showed no significant change in *MFN2* expression levels in EriR cells compared to parental

◂**Fig. 5** Activation of PERK with upregulation of microtubule acetylation promotes cell death in eribulin-resistant (EriR) cells. **A** Immunofluorescence analysis using confocal microscopy with mitochondria (mito, red; stained with MitoTracker Red CMXRos dye) and nucleus in Hs578T *ATAT1*-overexpressed eribulin-resistant (R + O/E) cells transfected with GFP-SEC61β (ER) with indicated drugs treatment (eribulin (Eri) 1 nM for 72 h, CCT020312 (CCT) 5 μM for last 12 h, (A)-(D)). The bar graph shows the Manders' overlap coefficient in R + O/E cells. Scale bar, 20 μm (left) and 2.5 μm (right). Statistical analysis was performed using one-way ANOVA with Tukey's multiple comparisons. One-way ANOVA, $F_{3, 96} = 3.213$. **B** The bar graph shows the intensity of Mito-GCaMP6f normalized to Mitotracker intensity in Hs578T R + O/E cells transfected with Mito-GCaMP6f with indicated drug treatment. One-way ANOVA, $F_{3, 156} = 32.91$. **C** Immunofluorescence analysis with cytochrome c (Cyt c, green), mitochondria (mito, red; stained with MitoTracker Red CMXRos dye), and nucleus (blue) in Hs578T R + O/E cells with indicated drugs. Scale bar, 20 μm. **D** Hs578T R + O/E cells were treated with indicated drugs. MTT assay was performed to measure the viability of cells. One-way ANOVA, $F_{3, 8} = 296.9$. **E** Immunofluorescence analysis using confocal microscopy with mito (stained with MitoTracker Red CMXRos dye) and nucleus in Hs578T eribulin-resistant (R) cells transfected with GFP-SEC61β (ER) with indicated drugs treatment (Eri and CCT described in (A) and tubacin (Tub) 0.5 μM for 72 h, (E–H). The bar graph shows the Manders' overlap coefficient in R cells. Scale bar, 20 μm (upper) and 2.5 μm (lower). One-way ANOVA, $F_{4, 120} = 10.20$. **F** The bar graph shows the intensity of Mito-GCaMP6f normalized to Mitotracker intensity in Hs578T R cells transfected with Mito-GCaMP6f with indicated drugs. One-way ANOVA, $F_{4, 95} = 28.25$. **G** Immunofluorescence analysis with Cyt c, mito (stained with MitoTracker Red CMXRos dye), and nucleus in Hs578T R cells with indicated drugs. Scale bar, 20 μm. **H** Hs578T parental (P) and R cells were treated with indicated drugs. MTT assay was performed to measure the viability of cells. One-way ANOVA, $F_{6, 14} = 78.77$. $^{**}p < 0.01$, $^{****}p < 0.0001$, n.s. not significant

cells (fold change = 0.862 and p-value = 0.084), suggesting that *MFN2* transcriptional downregulation is unlikely to be a major driver of eribulin resistance. Nevertheless, it is important to note that MFN2 function may also be regulated post-transcriptionally or through protein–protein interactions, which could influence its ability to recruit α-TAT1 to mediate ER-mitochondria contacts. Future studies should investigate MFN2 protein levels, localization, and interaction with α-TAT1 in EriR cells to determine whether these mechanisms are involved in modulating microtubule acetylation and mitochondrial dynamics. Notably, given the established role of acetylated microtubules in ER-mitochondrial contact, we observed an increase in these contacts after eribulin treatment and proceeded to investigate the functional interaction between the ER and mitochondria (Fig. 2). Although the precise molecular mechanisms underlying eribulin-induced ER-mitochondria tethering remain unclear, our results indicate that eribulin-induced microtubule acetylation reinforces the structural framework for ER-mitochondria contacts, facilitating Ca^{2+} transfer from the ER to the mitochondria, ultimately leading to cell death.

Microtubule acetylation and PERK activity are critical for eliminating EriR cells. While UPR signaling typically restores cellular homeostasis in response to ER stress, its hyperactivation during prolonged stress induces cell death [56]. Elevated ER stress through PERK activation has enhanced chemosensitivity to taxol, causing cell death in colorectal cancer cells [40]. Our results demonstrated that PERK downregulation reduced sensitivity to eribulin, similar to the effect of decreased microtubule acetylation (Fig. 4G, H). However, PERK activity and microtubule acetylation likely act independently in regulating eribulin sensitivity, as altering one did not affect the expression of the other (Figs. S7C, S11B). For example, in *ATAT1* KD cells, PERK was still partially activated by eribulin (Fig. S11B); however, increased distance between the ER and mitochondria reduced Ca^{2+} transfer to mitochondria, likely contributing to the lower sensitivity to eribulin. In contrast, in *ATAT1*-overexpressing EriR cells, additional PERK activation was required to induce cell death (Fig. 5A–D). PERK regulates Ca^{2+} transfer from the ER to mitochondria within MAMs [57]. For instance, Mfn2 deficiency, which disrupts ER-mitochondrial tethering, increases PERK phosphorylation and promotes mitochondrial Ca^{2+} overload, while PERK silencing reduces Ca^{2+} transfer to the mitochondria [24]. Additionally, PERK activation upregulates Sig-1R, promoting extended ER Ca^{2+} release and selectively Ca^{2+} transfer to the mitochondria [58, 59]. Further studies are needed to clarify the molecular mechanisms by which eribulin-activated PERK facilitates mitochondrial Ca^{2+} overload.

Prior research has highlighted the potential of HDAC6 inhibition to enhance the anti-tumor efficacy of eribulin through microtubule acetylation, suggesting a novel therapeutic strategy for TNBC. However, the precise molecular mechanisms are unclear [60]. The study investigated combination treatments using ricolinostat (RICO), an HDAC6 inhibitor, with eribulin in two ways: a low concentration of RICO with eribulin and pre-treatment with a high concentration of RICO. In the first case, the combination treatment partially reduced resistance to eribulin in eribulin-resistant cells but did not restore sensitivity to the level seen in the parental cells. Although the low concentration of RICO elevated microtubule acetylation, it was not sufficient on its own to overcome eribulin resistance, similar to our findings that overexpression of *ATAT1* did not overcome eribulin resistance in EriR cells (Fig. 3). In the second case, HDAC6 binds to various substrates, including α-tubulin, altering acetylation status of them [61]. Notably, in another study, the selective HDAC6 inhibitor ACY-1215 amplified acetylation on glucose-regulated protein 78, leading to its dissociation from PERK and subsequent activation of PERK signaling in OCI-Ly10 cells [62]. In line with our findings, HDAC6 inhibition with a high concentration of RICO likely enhances PERK activation, resulting in a synergistic effect on eribulin-induced cell death. The investigation of the role of microtubule acetylation in eribulin-induced cell death is

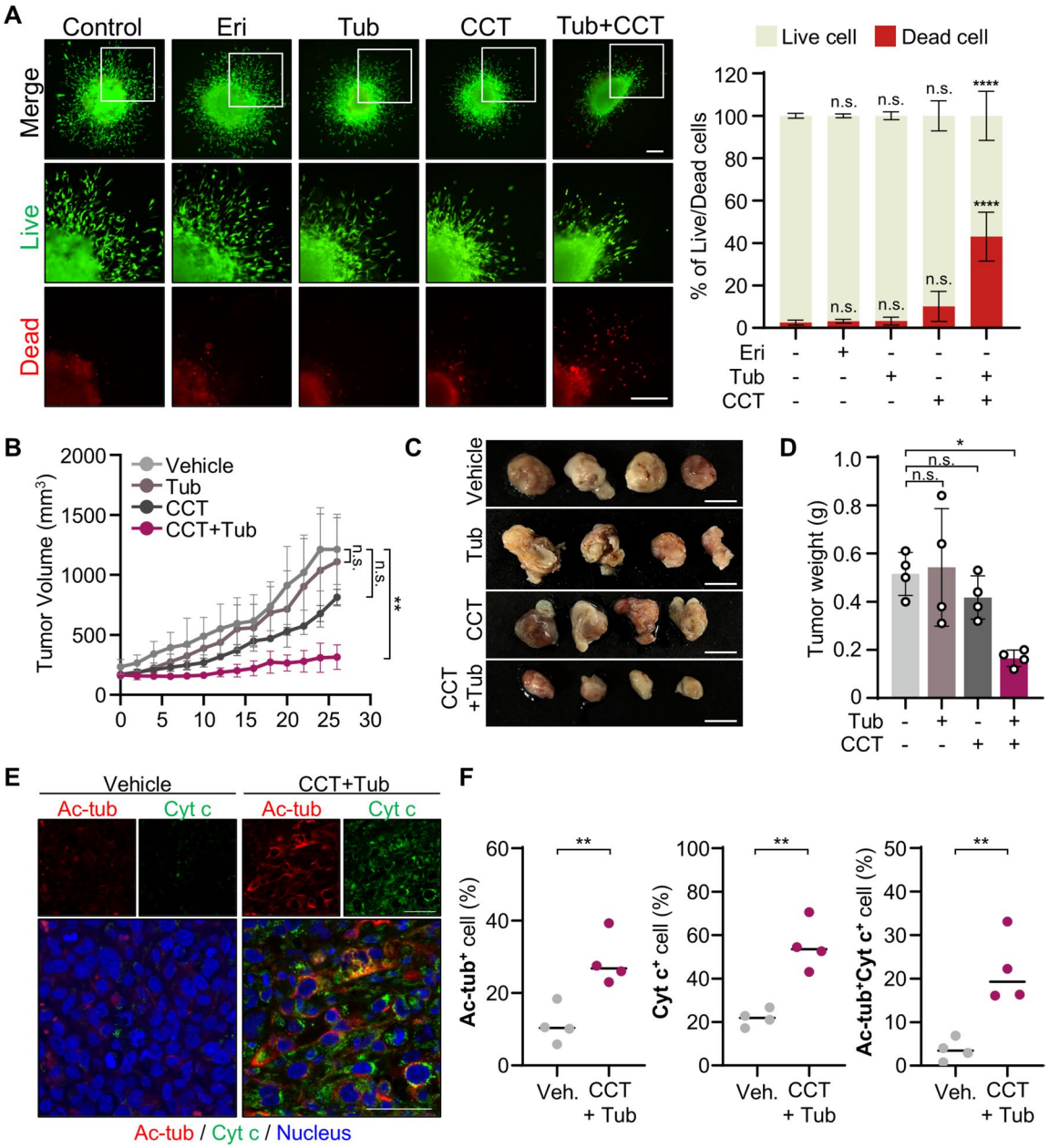

Fig. 6 Pharmacological induction of microtubule acetylation and PERK activity attenuates an eribulin-resistant (EriR) xenograft tumor growth. **A** Live/Dead assay for 3D spheroids of Hs578T eribulin-resistant (EriR) cells treated with eribulin (Eri) or tubacin (Tub) or CCT020312 (CCT) (Eri 1 nM and Tub 0.5 μM for 72 h, CCT 5 μM for last 12 h). Live cells are stained green (Calcein-AM), and dead cells are stained red (EthD-1). Scale bar, 250 μm. The bar graph shows the % of Live/Dead cells. Two-way ANOVA with Tukey's multiple comparisons test. **B** Growth curves of tumors after subcutaneous injection of MDA-MB-231 (MDA-231) EriR cells followed by treatment of CCT020312 (CCT, 2 mg/kg every four days via intraperitoneal injection (i.p.)) or tubacin (Tub, 0.5 mg/kg every day via i.p.) for 26 days. The tumor volume was measured every 2 days, and the tumors were dissected at the endpoint of the experiments (n = 4 mice per group). One-way ANOVA, $F_{3,\ 12} = 10.95$. **C** Representative image of growing tumors in each group. Scale bar, 1 cm. **D** Measurement of tumor weights at 26 days in each group. One-way ANOVA, $F_{3,\ 12} = 6.175$. **E** Immunohistochemical (IHC) analysis of acetylated tubulin (Ac-tub, red), cytochrome c (Cyt c, green), and nucleus (blue) in tumor sections obtained from MDA-231 EriR xenograft mice treated with or without combination of CCT and Tub. Scale bar, 50 μm. **F** Quantification of Ac-tub or Cyt c positive cells (Ac-tub$^+$ or Cyt c$^+$ (%)) in IHC analysis of endpoint tumors described in **A**. Statistical analysis was performed using the student's unpaired t-test. $*p < 0.05$, $**p < 0.01$, $****p < 0.0001$, n.s. not significant

aligned with our research. However, we have newly discovered that eribulin-induced microtubule acetylation enhances ER-mitochondria contacts and PERK activation increases Ca^{2+} transfer from ER to the mitochondria, effectively promoting cell death in EriR cells. Taken together, we propose that simultaneously activating both microtubule acetylation and PERK may represent a more effective therapeutic strategy for treating eribulin-resistant breast cancer.

This study demonstrates that microtubule acetylation is crucial in facilitating Ca^{2+} transfer between the ER and mitochondria, highlighting the importance of structural coordination in this process. We also found that PERK activation is essential for amplifying Ca^{2+} transfer following eribulin treatment. Notably, the combined increase in microtubule acetylation and PERK activity was sufficient for cell death in EriR cells. Given that drug resistance remains a significant challenge in cancer therapy, our findings suggest that targeting the microtubule acetylation-driven ER-mitochondria Ca^{2+} transfer mechanism could be a promising approach for overcoming resistance to other anticancer drugs.

Supplementary Information The online version contains supplementary material available at https://doi.org/10.1007/s00018-024-05565-w.

Acknowledgements We thank Professor Chao Tong (Zhejiang University, China) for providing plx304-spGFP1-10-ERt and pLVX-Mitot-l2-2xspGFP11 constructs, which were used to analyze the changes in contacts between the ER and mitochondria.

Author contributions SS, PK, and SR conceptualized this study. SS and SR drafted the manuscript. SS, PK, SK, and JJ performed the experiments and analyzed the data. SS and YEH contributed to the animal experiments. PK, JJ, and J-HC provided resources for cell-based and molecular experiments, helped generate figures, and interpreted the experimental data. ML discussed all the data. Y-SJ and SHK contributed to the experimental design, reviewed the manuscript, and provided scientific input. SR supervised and administered the study. All the authors critically revised and approved the final version of the manuscript.

Funding This research was supported by grants from the National Research Foundation of Korea (NRF), funded by the Korean Government (MSIT) (No. RS-2024-00348828 and RS-2023-00220089).

Data availability All data and materials used during this research are available from the corresponding author upon reasonable request.

Declarations

Conflict of interests The authors declare no competing interests.

Ethical approval The experimental procedures with animals were approved by the Institutional Animal Care and Use Committee of Chung-Ang University (Approval ID: 2019-00133).

Consent to participate Not applicable.

Consent to publish Not applicable.

References

1. Ferreira JG, Pereira AL, Maiato H (2014) Microtubule plus-end tracking proteins and their roles in cell division. Int Rev Cell Mol Biol 309(309):59–140
2. Parker AL, Kavallaris M, McCarroll JA (2014) Microtubules and their role in cellular stress in cancer. Front Oncol 4:153
3. Tikhomirova MS, Kadosh A, Saukko-Paavola AJ, Shemesh T, Klemm RW (2022) A role for endoplasmic reticulum dynamics in the cellular distribution of microtubules. Proc Natl Acad Sci U S A 119:e2104309119
4. Janke C, Magiera MM (2020) The tubulin code and its role in controlling microtubule properties and functions. Nat Rev Mol Cell Biol 21:307–326
5. Friedman JR, Webster BM, Mastronarde DN, Verhey KJ, Voeltz GK (2010) ER sliding dynamics and ER-mitochondrial contacts occur on acetylated microtubules. J Cell Biol 190:363–375
6. Ko P, Choi JH, Song S, Keum S, Jeong J, Hwang YE, Kim JW, Rhee S (2021) Microtubule acetylation controls MDA-MB-231 breast cancer cell invasion through the modulation of endoplasmic reticulum stress. Int J Mol Sci 22:6018
7. Jeong J, Kim OH, Shim J, Keum S, Hwang YE, Song S, Kim JW, Choi JH, Lee HJ, Rhee S (2023) Microtubule acetylation induced by oxidative stress regulates subcellular distribution of lysosomal vesicles for amyloid-beta secretion. J Cell Physiol 238:2812–2826
8. Wang X, Gigant B, Zheng X, Chen Q (2023) Microtubule-targeting agents for cancer treatment: seven binding sites and three strategies. MedComm Oncol 2:46
9. Romeo V, Accardo G, Perillo T, Basso L, Garbino N, Nicolai E, Maurea S, Salvatore M (2021) Assessment and prediction of response to neoadjuvant chemotherapy in breast cancer: a comparison of imaging modalities and future perspectives. Cancers (Basel) 13:3521
10. An J, Peng C, Tang H, Liu X, Peng F (2021) New advances in the research of resistance to neoadjuvant chemotherapy in breast cancer. Int J Mol Sci 22:9644
11. Si W, Shen J, Zheng H, Fan W (2019) The role and mechanisms of action of microRNAs in cancer drug resistance. Clin Epigenetics 11:25
12. Kinnel B, Singh SK, Oprea-Ilies G, Singh R (2023) Targeted therapy and mechanisms of drug resistance in breast cancer. Cancers (Basel) 15:1320
13. Shima H, Yamada A, Ishikawa T, Endo I (2017) Are breast cancer stem cells the key to resolving clinical issues in breast cancer therapy? Gland Surg 6:82–88
14. Liu XY, Jiang W, Ma D, Ge LP, Yang YS, Gou ZC, Xu XE, Shao ZM, Jiang YZ (2020) SYTL4 downregulates microtubule stability and confers paclitaxel resistance in triple-negative breast cancer. Theranostics 10:10940–10956

15. Jimenez PC, Wilke DV, Costa-Lotufo LV (2018) Marine drugs for cancer: surfacing biotechnological innovations from the oceans. Clinics (Sao Paulo) 73:e482s
16. Kikawa Y, Kotake T, Tsuyuki S, Kang Y, Takahara S, Fujimoto Y, Yamashiro H, Yoshibayashi H, Takada M, Yasuoka R et al (2022) Effectiveness of eribulin as first-line or second-line chemotherapy for HER2-negative hormone-resistant advanced or metastatic breast cancer: findings from the multi-institutional, prospective, observational KBCRN A001: E-SPEC study. Breast Cancer 29:796–807
17. Twelves C, Jove M, Gombos A, Awada A (2016) Cytotoxic chemotherapy: Still the mainstay of clinical practice for all subtypes metastatic breast cancer. Crit Rev Oncol Hematol 100:74–87
18. Gordaliza-Alaguero I, Canto C, Zorzano A (2019) Metabolic implications of organelle-mitochondria communication. EMBO Rep 20:e47928
19. Lackner LL (2019) The expanding and unexpected functions of mitochondria contact sites. Trends Cell Biol 29:580–590
20. Carpio MA, Means RE, Brill AL, Sainz A, Ehrlich BE, Katz SG (2021) BOK controls apoptosis by Ca(2+) transfer through ER-mitochondrial contact sites. Cell Rep 34:108827
21. Kerkhofs M, Bittremieux M, Morciano G, Giorgi C, Pinton P, Parys JB, Bultynck G (2018) Emerging molecular mechanisms in chemotherapy: Ca(2+) signaling at the mitochondria-associated endoplasmic reticulum membranes. Cell Death Dis 9:334
22. Doghman-Bouguerra M, Granatiero V, Sbiera S, Sbiera I, Lacas-Gervais S, Brau F, Fassnacht M, Rizzuto R, Lalli E (2016) FATE1 antagonizes calcium- and drug-induced apoptosis by uncoupling ER and mitochondria. EMBO Rep 17:1264–1280
23. Chen X, Shi C, He M, Xiong S, Xia X (2023) Endoplasmic reticulum stress: molecular mechanism and therapeutic targets. Signal Transduct Target Ther 8:352
24. Munoz JP, Ivanova S, Sanchez-Wandelmer J, Martinez-Cristobal P, Noguera E, Sancho A, Diaz-Ramos A, Hernandez-Alvarez MI, Sebastian D, Mauvezin C et al (2013) Mfn2 modulates the UPR and mitochondrial function via repression of PERK. EMBO J 32:2348–2361
25. Carreras-Sureda A, Jana F, Urra H, Durand S, Mortenson DE, Sagredo A, Bustos G, Hazari Y, Ramos-Fernandez E, Sassano ML et al (2019) Non-canonical function of IRE1alpha determines mitochondria-associated endoplasmic reticulum composition to control calcium transfer and bioenergetics. Nat Cell Biol 21:755–767
26. Erie C, Sacino M, Houle L, Lu ML, Wei J (2015) Altered lysosomal positioning affects lysosomal functions in a cellular model of Huntington's disease. Eur J Neurosci 42:1941–1951
27. Lee KS, Huh S, Lee S, Wu Z, Kim AK, Kang HY, Lu B (2018) Altered ER-mitochondria contact impacts mitochondria calcium homeostasis and contributes to neurodegeneration in vivo in disease models. Proc Natl Acad Sci U S A 115:E8844–E8853
28. You E, Ko P, Jeong J, Keum S, Kim JW, Seo YJ, Song WK, Rhee S (2020) Dynein-mediated nuclear translocation of yes-associated protein through microtubule acetylation controls fibroblast activation. Cell Mol Life Sci 77:4143–4161
29. Rhee S, Grinnell F (2006) P21-activated kinase 1: convergence point in PDGF- and LPA-stimulated collagen matrix contraction by human fibroblasts. J Cell Biol 172:423–432
30. Goto W, Kashiwagi S, Asano Y, Takada K, Takahashi K, Fujita H, Takashima T, Shibutani M, Amano R, Tomita S et al (2019) The effects of eribulin on breast cancer microenvironment identified using eribulin-resistant breast cancer cell lines. Anticancer Res 39:4031–4041
31. Okouneva T, Azarenko O, Wilson L, Littlefield BA, Jordan MA (2008) Inhibition of centromere dynamics by eribulin (E7389) during mitotic metaphase. Mol Cancer Ther 7:2003–2011
32. Lopes D, Seabra AL, Orr B, Maiato H (2023) alpha-Tubulin detyrosination links the suppression of MCAK activity with taxol cytotoxicity. J Cell Biol 222:e202205092
33. Yang Z, Zhao X, Xu J, Shang W, Tong C (2018) A novel fluorescent reporter detects plastic remodeling of mitochondria-ER contact sites. J Cell Sci 131:jcs208686
34. de Juan-Sanz J, Holt GT, Schreiter ER, de Juan F, Kim DS, Ryan TA (2017) Axonal endoplasmic reticulum Ca(2+) content controls release probability in CNS nerve terminals. Neuron 93(867–881):e866
35. Mateus D, Marini ES, Progida C, Bakke O (2018) Rab7a modulates ER stress and ER morphology. Biochim Biophys Acta Mol Cell Res 1865:781–793
36. Carter RJ, Milani M, Beckett AJ, Liu S, Prior IA, Cohen GM, Varadarajan S (2022) Novel roles of RTN4 and CLIMP-63 in regulating mitochondrial structure, bioenergetics and apoptosis. Cell Death Dis 13:436
37. Shrestha N, Torres M, Zhang J, Lu Y, Haataja L, Reinert RB, Knupp J, Chen YJ, Parlakgul G, Arruda AP et al (2023) Integration of ER protein quality control mechanisms defines beta cell function and ER architecture. J Clin Invest 133:163584
38. Hetz C (2012) The unfolded protein response: controlling cell fate decisions under ER stress and beyond. Nat Rev Mol Cell Biol 13:89–102
39. van Vliet AR, Giordano F, Gerlo S, Segura I, Van Eygen S, Molenberghs G, Rocha S, Houcine A, Derua R, Verfaillie T et al (2017) The ER stress sensor PERK coordinates ER-plasma membrane contact site formation through interaction with filamin-A and F-actin remodeling. Mol Cell 65(885–899):e886
40. Lei Y, He L, Yan C, Wang Y, Lv G (2021) PERK activation by CCT020312 chemosensitizes colorectal cancer through inducing apoptosis regulated by ER stress. Biochem Biophys Res Commun 557:316–322
41. Jaaks P, Coker EA, Vis DJ, Edwards O, Carpenter EF, Leto SM, Dwane L, Sassi F, Lightfoot H, Barthorpe S et al (2022) Effective drug combinations in breast, colon and pancreatic cancer cells. Nature 603:166–173
42. Nomura Y, Nakano M, Woo Sung H, Han M, Pandey D (2021) Inhibition of HDAC6 activity protects against endothelial dysfunction and atherogenesis in vivo: a role for HDAC6 neddylation. Front Physiol 12:675724
43. Ota S, Zhou ZQ, Hurlin PJ (2018) Suppression of FGFR3- and MYC-dependent oncogenesis by tubacin: association with HDAC6-dependent and independent activities. Oncotarget 9:3172–3187
44. Mackeh R, Lorin S, Ratier A, Mejdoubi-Charef N, Baillet A, Bruneel A, Hamai A, Codogno P, Pous C, Perdiz D (2014) Reactive oxygen species, AMP-activated protein kinase, and the transcription cofactor p300 regulate alpha-tubulin acetyltransferase-1 (alphaTAT-1/MEC-17)-dependent microtubule hyperacetylation during cell stress. J Biol Chem 289:11816–11828
45. Xiao H, Verdier-Pinard P, Fernandez-Fuentes N, Burd B, Angeletti R, Fiser A, Horwitz SB, Orr GA (2006) Insights into the mechanism of microtubule stabilization by Taxol. Proc Natl Acad Sci U S A 103:10166–10173
46. Eshun-Wilson L, Zhang R, Portran D, Nachury MV, Toso DB, Lohr T, Vendruscolo M, Bonomi M, Fraser JS, Nogales E (2019) Effects of alpha-tubulin acetylation on microtubule structure and stability. Proc Natl Acad Sci U S A 116:10366–10371
47. Liu W, Wang C, Yu H, Liu S, Yang J (2018) Expression of acetylated tubulin in the postnatal developing mouse cochlea. Eur J Histochem 62:2942
48. Doodhi H, Prota AE, Rodriguez-Garcia R, Xiao H, Custar DW, Bargsten K, Katrukha EA, Hilbert M, Hua S, Jiang K et al (2016) Termination of protofilament elongation by eribulin induces

lattice defects that promote microtubule catastrophes. Curr Biol 26:1713–1721
49. Shah N, Kumar S, Zaman N, Pan CC, Bloodworth JC, Lei W, Streicher JM, Hempel N, Mythreye K, Lee NY (2018) TAK1 activation of alpha-TAT1 and microtubule hyperacetylation control AKT signaling and cell growth. Nat Commun 9:1696
50. You E, Jeong J, Lee J, Keum S, Hwang YE, Choi JH, Rhee S (2022) Casein kinase 2 promotes the TGF-beta-induced activation of alpha-tubulin acetyltransferase 1 in fibroblasts cultured on a soft matrix. BMB Rep 55:192–197
51. Vona R, Mileo AM, Matarrese P (2021) Microtubule-based mitochondrial dynamics as a valuable therapeutic target in cancer. Cancers (Basel) 13:5812
52. Canty JT, Hensley A, Aslan M, Jack A, Yildiz A (2023) TRAK adaptors regulate the recruitment and activation of dynein and kinesin in mitochondrial transport. Nat Commun 14:1376
53. Balabanian L, Berger CL, Hendricks AG (2017) Acetylated microtubules are preferentially bundled leading to enhanced kinesin-1 motility. Biophys J 113:1551–1560
54. Dompierre JP, Godin JD, Charrin BC, Cordelieres FP, King SJ, Humbert S, Saudou F (2007) Histone deacetylase 6 inhibition compensates for the transport deficit in Huntington's disease by increasing tubulin acetylation. J Neurosci 27:3571–3583
55. Kumar A, Larrea D, Pero ME, Infante P, Conenna M, Shin GJ, Van Elias V, Grueber WB, Di Marcotullio L, Area-Gomez E et al (2024) MFN2 coordinates mitochondria motility with alpha-tubulin acetylation and this regulation is disrupted in CMT2A. Science 27:109994
56. Kim I, Xu W, Reed JC (2008) Cell death and endoplasmic reticulum stress: disease relevance and therapeutic opportunities. Nat Rev Drug Discov 7:1013–1030
57. Fan P, Jordan VC (2022) PERK, beyond an unfolded protein response sensor in estrogen-induced apoptosis in endocrine-resistant breast cancer. Mol Cancer Res 20:193–201
58. Kumar V, Maity S (2021) ER stress-sensor proteins and er-mitochondrial crosstalk-signaling beyond (ER) stress response. Biomolecules 11:173
59. Hayashi T, Su TP (2007) Sigma-1 receptor chaperones at the ER-mitochondrion interface regulate Ca(2+) signaling and cell survival. Cell 131:596–610
60. Oba T, Ono M, Matoba H, Uehara T, Hasegawa Y, Ito KI (2021) HDAC6 inhibition enhances the anti-tumor effect of eribulin through tubulin acetylation in triple-negative breast cancer cells. Breast Cancer Res Treat 186:37–51
61. Gomes ID, Ariyaratne UV, Pflum MKH (2021) HDAC6 substrate discovery using proteomics-based substrate trapping: HDAC6 Deacetylates PRMT5 to influence methyltransferase activity. ACS Chem Biol 16:1435–1444
62. Amengual JE, Johannet P, Lombardo M, Zullo K, Hoehn D, Bhagat G, Scotto L, Jirau-Serrano X, Radeski D, Heinen J et al (2015) Dual targeting of protein degradation pathways with the selective HDAC6 Inhibitor ACY-1215 and bortezomib is synergistic in lymphoma. Clin Cancer Res 21:4663–4675